Rev. Roum. Sci. Techn.– Électrotechn. et Énerg.
Vol. **69**, *1*, pp. 115–120, Bucarest, 2024

DEEP VEIN NET: DEEP VEIN THROMBOSIS IDENTIFICATION VIA SOOTY TERN OPTIMIZED DEEP LEARNING NETWORK

BASTIN ROGERS CROSS JOSEPH[1], IMMANUEL JOHNRAJA JEBADURAI[2], GETZI JEBA LEELIPUSHPAM PAULRAJ[3], JEBAVEERASINGH JEBADURAI[4], MULLI MARY VARUVEL[5]

Keywords: **Deep vein thrombosis; Deep learning; Discrete wavelet transform; Dilated convolutional neural network; Sooty tern optimization algorithm.**

Deep vein thrombosis (DVT) occurs when thrombosis (blood clots) forms in veins far below the skin's surface due to veins or sluggish blood flow injuries. An obstruction in blood flow through a vein could be partially or completely caused by blood clots. DVTs typically occur in the thigh, lower leg, or pelvis, yet can also occur in other body parts, such as the brain, liver, intestines, arm, or kidney. This research proposes a novel Deep Vein Net, integrating deep learning-based dilated CNN and Sooty Tern optimization to detect DVT from CT and MRI images efficiently. The input CT and MRI images are pre-processed to eliminate noise artifacts using the Discrete Wavelet Transform (DWT). Furthermore, the pre-processed images are fed into a Dilated convolutional neural network (Dilated CNN) for feature extraction to extract the most pertinent features. Lastly, the STO algorithm uses the fuzzy Extreme Learning Machine of thrombosis stages normal and DVT to select the best features for additional classification. Metrics like rec, spe, acc, pre, and F1 scores were used to assess the Deep Vein Net's performance. The suggested method achieves a classification accuracy of 99.25 % when identifying DVT cases.

1. INTRODUCTION

A deep vein thrombus (DVT) develops when blood flows too slowly through veins deep in the body due to injuries or sluggish veins [1]. Venous thromboembolism (VTE) is linked to a considerable burden of disease on a global scale. Its prevalence worldwide stands at 1–3 cases per 1000 individuals, rising to 2.7 per 1000 among individuals over 70 and reaching 3.1 per 1000 among those over 80. The primary contributors to hospital-related disability-adjusted life years lost are pulmonary embolism (PE), DVT, and VTE [2]. Up to 30% of DVT patients are symptom-free, while symptoms can be very minimal or no cause for concern [3]. Before the blood clot from the arm or leg reaches the lungs, some patients don't realize they have DVT [4]. Any age can experience severe DVT or PE. However, children and teenagers experience it less frequently, while adults over 60 experience it more frequently [5].

However, the similar symptoms present in many other disorders make clinical identification of this illness difficult [6, 7]. Vessels become hyperintense on CTA images because of the iodinated contrast agent's amplification, while PE appears as dark patches [8]. Radiologists commonly perform CTA readings. However, visual detection of PE in CTA images is regarded as laborious, arbitrary, and misdiagnosed [9,10]. The goal of this research is to better diagnose PE, lower the cost of patient care, and enhance therapy [11]. A deep neural network model [12] with visual morphology is used to automatically detect pulmonary embolisms (PE). DL can extract features automatically compared to relying on human features [13]. Utilizing deep learning algorithms, particularly dilated CNN, for detecting and classifying DVT from medical images has gained attention due to its potential to offer faster, more accurate, and cost-effective diagnostic solutions. The research paper proposed a Sooty Tern Optimization Algorithm (STOA) based on the deep learning technique to automatically identify the DVT in CT and MRI images [20–22]. The main contribution of the paper is summarized as:

- The primary purpose of the work is to represent a novel Deep Vein Net that has been proposed to identify DVT in CT and MRI images.
- Initially, the input CT and MRI images are Pre-processed using the DWT to remove the noise artifacts.
- Then, the denoised images are given as input to the feature extraction using a dilated convolutional neural network (dilated CNN) for extracting the most relevant features.
- The relevant features of CT and MRI images are selected using the STO Algorithm.
- The fuzzy extreme learning machine to classify the normal and DVT cases.

The remainder of the paper was segmented into five main sections. Section 2 encompasses the related works, section 3 delves into the proposed Deep Vein Net discussion, section 4 presents the experimental results and subsequent discussion, and section 5 addresses the conclusion and outlines future work.

2. LITERATURE SURVEY

Researchers have recently presented a number of methods and techniques, primarily aimed at effectively identifying cases of DVT. Some of those feature extraction, feature selection, and classification techniques are studied briefly in this section.

Reference [14] suggested using two image analysis techniques to spot DVT in kids. To identify the thrombus, the CT scans must first be segmented by thresholding the image. The next step is to find the thrombus's border. After using the entropy-thresholding method to finish the first stage, the active contours approach was applied for the second stage.

Reference [15] proposed the PE-Deep Net (pulmonary embolism detection using deep neural networks) hybrid deep learning CNN model for pulmonary embolism diagnosis. It uses a common dataset of chest CT scan images for pulmonary embolisms from the RSNA.

Reference [16] suggested using deep learning to recognize pulmonary embolisms (PE) in CTA images. CTA images were first processed with a median filter to remove noise and

---

[1] Stella Mary's College of Engineering, Tamil Nadu, India. Corresponding author: bastinrogers@karunya.edu.in
[2] Karunya Institute of Technology and Sciences, Coimbatore, India. E-mail: immanueljohnraja@karunya.edu
[3] Karunya Institute of Technology and Sciences, Coimbatore, India. E-mail: getzi@karunya.edu
[4] Government Polytechnic College, Gandarvakottai, Tamil Nadu, India
[5] Arunachala College of Engineering for Women, Tamil Nadu, India

DOI: 10.59277/RRST-EE.2024.69.1.20

improve image quality. Next, to distinguish between PE and non-PE, we used TL techniques to implement two pre-trained CNN models, VGG-19 and Inception-V3.

Reference [17] proposed a deep learning architecture based on DenseNet201 for classifying PEs on CT images into nine classes. A fully connected decision plane was tuned and DenseNet201 was used as the feature extractor.

Reference [18] developed a CAD triage system to early detect PE patients. A model-ensemble design was suggested for the classification step to improve precision, and a different DRN was used to lessen false positive results in non-PE patients. The proposed model contained many innovative mechanisms for segmentation that could accurately label PE lesions with larger mIoU than previous techniques.

Reference [19] used machine learning techniques to develop a new predictive model for early childhood and adulthood. Using machine learning techniques, we compared clinical datasets of 406 subjects without DVT or PE and 167 patients with DVT and PE.

In the above-mentioned techniques, the classification process was not carried out to differentiate the healthy and DVT patients. To overcome this problem, the proposed Deep Vein Net method classifies the DVT and normal cases.

3. **PROPOSED DEEP VEIN NET**

In this paper, the proposed method is to identify DVT patients using CT and MRI images. This section is based on four phases: preprocessing, feature extraction, feature selection, and classification.

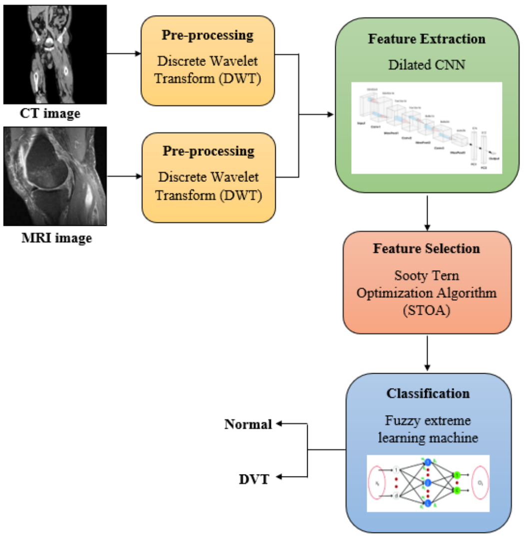

Fig. 1 – Schematic representation of proposed methodology.

The input CT and MRI images are Pre-processed using the DWT to remove the noise artifacts. Then, the pre-processed images are given as input to the feature extraction using dilated CNN for extracting the most relevant features. The STOA is used to select the relevant features of CT and MRI images. The fuzzy extreme learning machine to classify the normal and DVT cases. A flow diagram of the proposed model is shown in Fig. 1.

3.1. DATASET DESCRIPTION

The PE diagnosis dataset resulted from a collaboration between the Radiological Society of North America (RSNA) and the Society of Thoracic Radiology (STR). The employed method was CT angiography of the pulmonary arteries, also known as computed tomography of the chest images (CTPA). For this research, we focused on utilizing two labels (Acute PE and Chronic PE) with binary classification for annotation. A total of 9446 CTPA exams were conducted, with 7279 sets used for training. The image files were in DICOM format (dcm), featuring a resolution of 512×512 pixels.

3.2. PRE-PROCESSING

The image contains a noise of different sizes in the high and low-frequency areas. This noise is removed using a wavelet transform. The 2D DWT is used to create images with four frequency subbands (LL, LH, HL, and HH). It contains detailed sub-band images (LH, HH, and HL) and one approximate sub-band image (LL).

The original image is removed using wavelet noise reduction. Both hard and soft thresholds can be used in wavelet thresholding. By considering that noise is produced when the threshold value R exceeds the absolute value λ, the hard thresholding approach eliminates coefficients:

$$\hat{\lambda}_{hard} = \begin{cases} \lambda, & |\lambda| > T \\ 0, & |\lambda| \le T \end{cases} . \tag{1}$$

where the wavelet coefficient after shrinking is applied is represented by $\hat{\lambda}_{hard}$. Threshold value $T = \sigma\sqrt{2\log(N)}$, and the number of samples is denoted by N. When the absolute value λ is lower than the threshold value T, soft thresholding eliminates the wavelet coefficient; conversely, when the opposite is true, it reduces the coefficient by Equation (2). Details about soft thresholding are provided by,

$$\hat{\lambda}_{soft} = \begin{cases} \operatorname{sign}(\lambda)(|\lambda|), & |\lambda| > R, \\ 0, & |\lambda| \le R. \end{cases} \tag{2}$$

where the signum function sign(·)and after performing shrinking, the wavelet coefficient is $\hat{\lambda}_{soft}$.

Edge preservation may perform better with hard thresholding than with soft thresholding, although noise is a high-frequency element of the image (such as edge regions). Use soft thresholding instead of hard thresholding to maintain the edge regions and the speckle noise. Hard thresholding retains coefficients whose absolute values are the same as the threshold value, *T*. A Gibbs phenomenon takes place because the signal becomes discontinuous close to *T*. That is, because the tiny coefficient in this situation is 0, the variance is higher and thus more unstable than it would be with soft thresholding. Soft thresholding was used to eliminate the noise to achieve continuous noise reduction without increasing variance.

3.3. FEATURE EXTRACTION

Then, the denoised images are given as input to the feature extraction using Dilated Convolutional Neural Network (Dilated CNN) for extracting the most relevant features. The normal convolutional neural network (CNN) was replaced by the dilated convolutional neural network (DCNN).

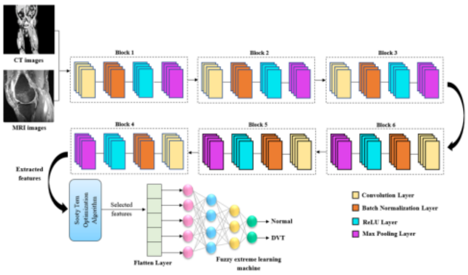

Fig. 2 – Architecture of the proposed Deep Vein Net model.

The dilated CNN employs larger 2-D filters. More compact convolution filters are frequently used in conventional CNNs. DCNNs use larger filters called dilated convolution filters. The CNN's receiving field is augmented by advanced convolutional filters without the need for additional context. This avoids the overfitting problem caused by deep CNNs and allows the augmented CNN to reach the received size of the field a few slices less than the CNN. Figure 2 illustrates the dilated CNN architecture.

A 28-layer design and six blocks from the base of the proposed Dilated CNN. The input image is specified to have dimensions of 512×256×3. Secondly, the convolution layer moves a window across the collected images in a stride to perform the convolution operation. A 5x5 window was built for the first convolution layer and utilized to convolve the pictures. There were 16 filters initially, and when more convolutional layers were added, the quantity of filtering grew. The receptive fields of the C2, C3, C4, C5, and C6 layers were increased using dilation factors. To avoid overfitting, the output of the preceding layer was normalized using batch normalization.

Batch normalization enables the layers of the system to learn independently. Before convolution, the rectified linear unit is utilized, and the feature maps produced are sent to the batch normalization layer using the formula $f(y) = \max(0,y)$. Fundamentally, using the function $f(y)$ means zeroing out the values of the neurons in a certain region. The feature layer's size can be decreased by max pooling each feature map in 2×2 steps.

Input Layer. Images are sent to the system by an image input layer. The form color channels, image height, and image width are the inputs for a DCNN. In the above-mentioned design, an image's width, height, and number of color channels are 512, 256, and 3, respectively.

Convolution Layer. The convolutional layer transfers the initial layer's features to a feature map, which is utilized to find local conjunctions of those features. In this layer, there is a filter that modifies the received image. The dilated convolution increases the dilated rate, which causes the convolution kernel's extended receptive field. Augmented convolution enriches multiscale information by extending the convolution kernel's receptive field. When the expansion ratio is set to 1, the enlarged receptive field size remains at 1.

The input images were processed through six convolution layers to extract their characteristics, and the filter's m x m pixel size was expanded using an r dilation rate. The formula is used to determine the size of a dilated convolution's receptive field,

$$N = F_c + (F_c - 1)(P - 1). \tag{3}$$

N indicates the receptive field's size, and P represents the dilation factor's size. A convolution layer with a 5×5 kernel size and 16 feature mappings were utilized as the leading layer. A convolution layer with 32 feature maps, a 5×5 kernel, and an $R = 2$ dilation rate made up the second layer. A 5×5 kernel, an $R = 4$ dilation rate, and 64 feature mappings constitute the third convolution layer. Fourth convolution layer, with $R = 8$ dilation rate, 5×5 kernel size, and 128 feature maps. A fifth convolution layer with 128 feature mappings, a 5x5 kernel, and a dilation rate of $R = 16$ is used. The 256 feature maps are used in the sixth convolution layer, which has a 5×5 kernel and an $R = 32$ dilation rate.

Batch Normalization Layer. The total feature maps are obtained once the convolution process is complete, and they are then used as input for the batch normalizing layer. The system's layers can each learn independently because of batch normalization. It standardizes the input value y_j while drastically decreasing the accuracy of network initialization by first computing μD and σ_D^2 by a short batch size to CNN training. The following equation is then used to determine the normalized activations:

$$\widehat{y_j} = \frac{y_j - \mu D}{\sqrt{\sigma_D^2 + c}}. \tag{4}$$

The batch normalization layer's standardized results are kept in $\widehat{y_j}$. The ReLU activation function subsequently utilizes the batch normalization layer's output.

Rectified Linear Unit (Re LU). Every convolutional layer's activation function was a Re LU function, which improved the yield's nonlinearity. It is denoted as follows:

$$f(y) = \max(0, y). \tag{5}$$

Because it is a non-linear operation, positive input sends one result, whereas negative input transmits zero results. As the Re LU's gradients can only be zeros or ones, there are no finite alternatives for positive input values. As a result, the Re LU can evaluate effectively and produce outcomes with a respectable level of accuracy.

Pooling Layer (PL). The PL is used to reduce the number of parameters in the convolution field by performing dimension reduction. In the proposed method, max pooling was implemented with a kernel size of 2×2 and a stride of 2. The key features of convolutional layers are usually used to create feature maps by layers of max pooling. $W_1 \times H_1 \times D_1$ is the size of the input that the convolutional layer gives to the pooling layer. W_1 represents width, H_1 represents height, and D_1 represents depth. 2×2 kernel size and pooling layer window size for each block in step 2. $W_2 \times H_2 \times D_2$ are the sizes of the output pooling layers, where:

$$W_2 = (W_1 - E)/S + 1, \tag{6}$$

$$H_2 = \frac{(H_1 - E)}{S + 1 - E}, \tag{7}$$

$$D_2 = D_1. \tag{8}$$

3.4. FEATURE SELECTION

A high-dimensional feature space is used for feature selection (FS), which selects the best feature subset based on predefined criteria to minimize the amount of data. In addition, features that are redundant, irrelevant, and relevant make up a feature space. A method for picking a subset of the characteristics that are extracted from the MRI and CT scan is called FS. FS is widely used to eliminate superfluous features that are unrelated to the classification process and to classify important traits that were previously unknown. The STO algorithm, which selects the most pertinent features from dilated CNN using a feature selection algorithm, is inspired by the natural behaviors of seabirds. The retrieved features are fed into the STO algorithm (Fig. 3), which determines which features are most relevant.

a) Migrating Behavior. For a sooty tern (ST) to migrate successfully, it must meet these three requirements.

(i) *Collison avoidance*. To avoid conflicts between its surrounding search agents (SAs), such as sooty terns, a new SA position is computed.

$$S_{st} = M_{sa} \times Q_{st}(j), \tag{9}$$

where Q_{st} denotes SA's current location, j denotes the actual iteration, M_{sa} denotes SA's moment in the designated search space, and position S_{st} is the SA's avoidance position concerning other SA.

(ii) *Converge in the direction of best neighbor*. The SA moved in the direction of their closest neighbour to prevent collisions,

$$N_{st} = Y \times \left(Q_{best}(j) - Q_{st}(j)\right). \tag{10}$$

Whereas Q_{st} points in the direction of the best-fit search agent (important features), N_{st} describes each agent's various places, and Y is a random variable that indicates superior exploration. Y is obtained in this way:

$$Y = 0.5 \times R_{and}. \tag{11}$$

R_{and} in this instance is a random number that lies in the interval [0, 1].

(iii) *Updating the best search agent*. After all, the search agent can become the best search agent by positioning itself accordingly.

$$H_{st} = S_{st} + N_{st}. \tag{12}$$

In this case, the difference between the SA and the best-fit SA with high fitness values (relevant characteristics) is described by H_{st}.

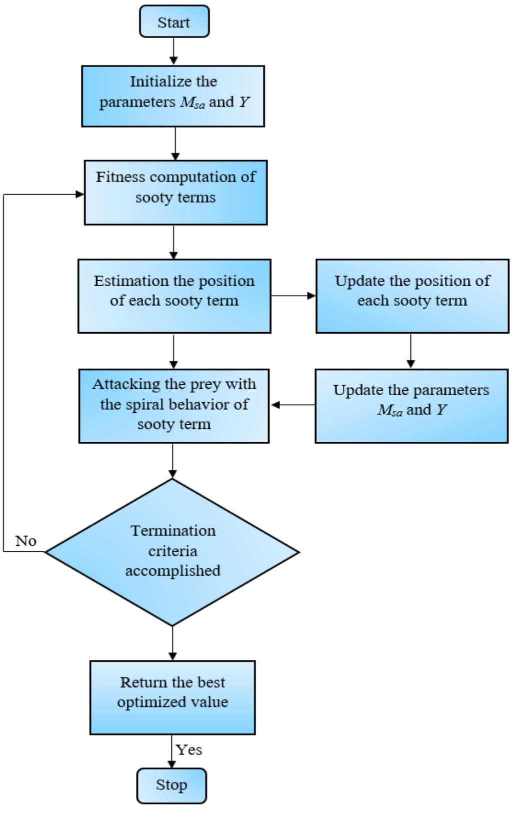

Fig. 3 – Flowchart of the STO algorithm.

b) Attacking behaviour. During migration, the ST can alter both its speed and attack angle. These birds can soar to greater heights because of their wings. When attacking prey in the air, sooty terns display spherical behavior. The mathematical derivation of this behavior is,

$$u = T_{radius} \times \sin(i), \tag{13}$$

$$v = T_{radius} \times \cos(i), \tag{14}$$

$$w = T_{radius} \times i, \tag{15}$$

$$t = c \times e^{kd}, \tag{16}$$

which indicates that the variable is inside the interval $\{0 \leq k \leq 2\pi\}$. The new position of SA is thus as follows, where c and d are constant values of 1:

$$Q_{st}(j) = \left(H_{st} \times (u + v + w)\right) \times Q_{best}(j). \tag{17}$$

Here, $Q_{st}(j)$ generates the best solution with the necessary properties by shifting the positions of other SA. The inputs are multiplied by the feature vectors, and then the randomly selected features are added. In the end, the STO algorithm is refined using the information obtained from attacking and migrating operations, and it can be fed into a fuzzy extreme learning machine to learn more about different categories.

3.5. CLASSIFICATION

The effects of the training points in classification problems should vary depending on the different weights. A set **M** of identified training points and related fuzzy memberships.

$$(y_1, r_1, m_1), \ldots., (y_n, r_n, m_n). \tag{18}$$

Individually training point y_j is assigned a label r_j and an uncertain membership $\sigma \leq m_j \leq 1$ small sufficiently with $\sigma > 0$. The fuzzy membership m_j is a view of the connected point y_j a single class and $\frac{1}{2}||\xi_j||$ is a measure of error, thus $\frac{1}{2}m_j||\xi_j||$ is an error measurement with various weights. The following approaches could be used to formulate the classification problem for the constrained optimal-based fuzzy ELM: minimize: $L_{FELM} = \frac{1}{2}||\beta||^2 + D\frac{1}{2}\sum_{j=1}^{N} m_j\,||\xi_j||^2$ subject to:

$$g(y_j)\beta = r_j^S - \xi_j^S, \qquad j = 1, \ldots\ldots N. \tag{19}$$

According to the KKT theorem, addressing the following dual optimization problem by fuzzy ELM training is comparable to,

$$\left(\frac{B}{C} + HH^s\right)\alpha = S, \tag{20}$$

$$\beta = H^s\left(\frac{B}{C} + HH^s\right)^{-1} S. \tag{21}$$

The learning of the output weights β can therefore be influenced in different ways by the inputs. Consequently, the FELM classifier's output function is

$$f(y) = g(y)\beta = f(y)H^s\left(\frac{B}{C} + HH^s\right)^{-1} S. \tag{22}$$

FELM only requires one output node for binary classification problems, and the decision function is

$$f(y) = \text{sign}\left(g(y)H^s\left(\frac{B}{C} + HH^s\right)^{-1} S\right). \tag{23}$$

In *n*-class scenarios, a testing point's predicted class label corresponds to the index number of the output node with the highest output value.

$$\text{label}(y) = \begin{cases} \arg\max g_i(y), \\ \ \ j \in \{1, \ldots n\} \end{cases}. \tag{24}$$

Furthermore, the fuzzy matrix **M** can be flexible-set to deal with various issues depending on different applications.

4. RESULTS AND DISCUSSION

This section uses Matlab-2019b to assess the suggested Deep Vein Net's efficiency. The raw CT and MRI images are taken from datasets that are openly accessible; they are first denoised into the appropriate frames for additional processing. Deep learning models are also compared with the suggested network.

Figure 4 demonstrates the experimental results of the proposed Deep Vein Net model using CT images. The input CT images (column 1) are denoised to eliminate the distortions (column 2). Dilated CNN uses these pre-processed images as input to extract features (column 3). Lastly, the process of classifying normal and DVT cases is carried out based on the features that have been chosen (column 4). Then, a similar process is repeated as in Fig. 5 using MRI images.

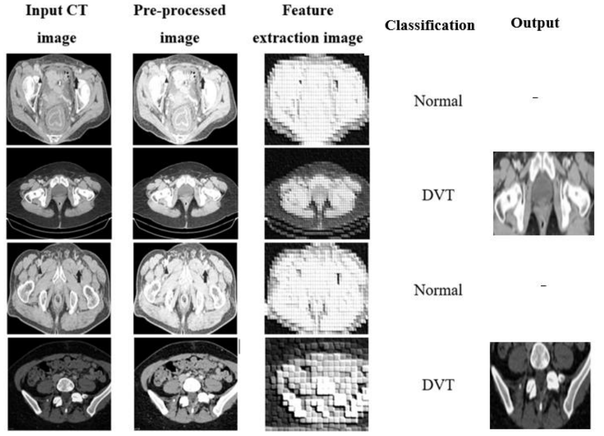

Fig. 4 –The experimental results of the proposed Deep Vein Net model using CT images.

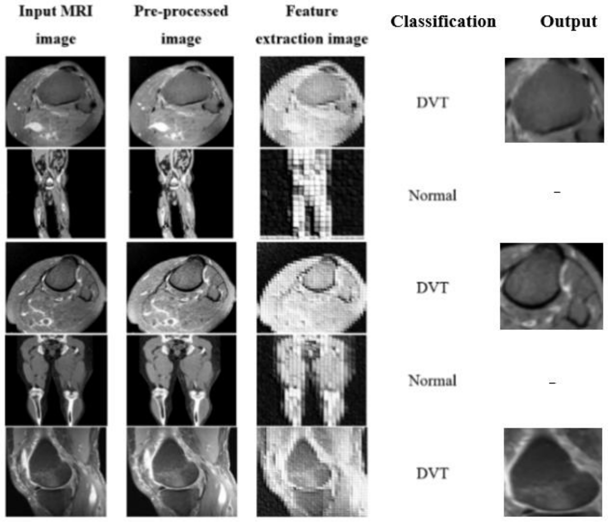

Fig. 5 – The experimental results of the proposed Deep Vein Net model using MRI images.

4.1. PERFORMANCE ANALYSIS

The efficiency of the proposed Deep Vein Net was assessed using the following particular metrics: F1 score, recall (rec), accuracy (acc), specificity (spe), and precision (pre).

$$\mathrm{acc} = \frac{\mathrm{TP+TN}}{\mathrm{TP+TN+FP+FN}}, \tag{25}$$

$$\mathrm{pre} = \frac{\mathrm{TP}}{\mathrm{TP+FP}}, \tag{26}$$

$$\mathrm{rec} = \frac{\mathrm{TP}}{\mathrm{TP+TN}}, \tag{27}$$

$$\mathrm{spe} = \frac{\mathrm{TN}}{\mathrm{TN+FP}}, \tag{28}$$

$$\mathrm{F1\ score} = 2\left(\frac{\mathrm{Precision-Recall}}{\mathrm{Precision+Recall}}\right), \tag{29}$$

where TP, FN, and FP stand for true and false positives and false negatives, respectively. Table 1 shows the effectiveness of the suggested Deep Vein Net method for classifying different DVT stages. It displays the classification efficiency of the proposed Deep Vein Net model for several types of DVT, including normal and DVT. Accuracy, recall, f1 score, precision, and specificity are used to assess competency. The accuracy of the suggested Deep Vein Net model is 99.25 %.

Table 1

The performance analysis of the proposed Deep Vein Net model

Classes	Acc	Pre	Rec	Spe	F1 score
Normal	99.25	98.24	98.74	97.24	98.04
DVT	98.18	97.14	97.23	96.08	97.02

The ROC calculated for the various DVT classes is displayed in Fig. 6. Based on TPR and FPR parameters, the suggested Deep Vein Net approach obtained an AUC of 0.992 for normal cases and 0.981 for DVT cases.

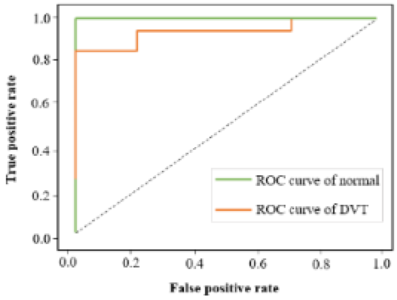

Fig. 6 – ROC curve of the proposed Deep Vein Net.

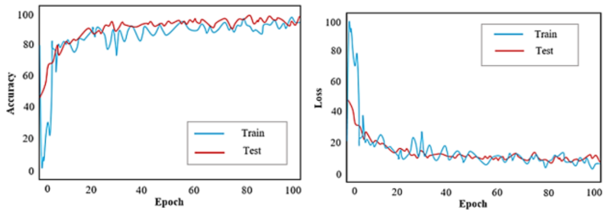

(a) (b)

Fig. 7 – a) Acc of the proposed Deep Vein Net; b) Loss of the proposed Deep Vein Net.

The acc chart is estimated using the acc range and 100 epochs in Fig. 7a. The accuracy of the suggested Deep Vein Net also advances as the number of epochs increases. The epochs and loss range are displayed in Fig. 7b, which indicates that the suggested Deep Vein Net's loss lowers when the epochs are increased. Using CT and MRI data, the suggested Deep Vein Net achieves great accuracy in identifying the various stages of DVT. In this study, many training epochs were initially computed to maximize testing accuracy. Based on the results, the suggested Deep Vein Net has a 99.25 % classification accuracy with a low error rate after 100 training epochs.

4.2. COMPARATIVE ANALYSIS

The performance of the proposed Deep Vein Net model and the existing method is examined in the comparative analysis section. The performance of the different deep-learning networks is assessed in this section.

The acc achieved by the proposed Deep Vein Net approach is 99.25 %, which is higher than the accuracy of the current deep learning networks. The proposed method performance is compared with the different deep learning networks such as Ghost Net, AlexNet, and Google Net.

The Proposed Deep Vein Net model enhances the total accuracy of the Ghost Net, AlexNet, and Google Net by 95.48 %, 96.32 %, and 98.46 % respectively. The Proposed Deep Vein Net model enhances the total specificity of the Ghost Net, AlexNet, and Google Net at 94.34 %, 95.59 %, and 96.18 % respectively.

The Proposed Deep Vein Net model enhances the total precision of the Ghost Net, AlexNet, and Google Net by 93.26 %, 94.27 %, and 95.08 % respectively. The Proposed Deep Vein Net method enhances the total recall of the Ghost Net, AlexNet, and Google Net in 91.74 %, 92.43 %, and 93.62 % respectively. The Proposed Deep Vein Net model enhances the total F1 score of Ghost Net, AlexNet, and Google Net by

92.17 %, 93.82 %, and 95.08 % respectively. The comparison of the existing and proposed model in Fig. 8.

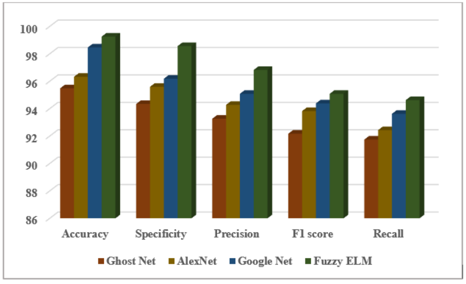

Fig. 8 – Comparison between existing and traditional deep learning techniques.

Table 2

Comparison of the existing versus proposed model

Authors	Methods	Accuracy
Lynch [15]	PE-Deep Net	94.2%
Khachnaoui [16]	Transfer Learning	90.50%
Yu [18]	DRN	85%
Proposed	Deep Vein Net	99.25%

Table 2 compares existing models with high classification accuracy using different metrics. The Deep Vein Net advances the overall accuracy by 5.08%, 8.81%, and 14.35% better than PE-Deep Net [15], Transfer Learning [16], and DRN [18], respectively. Table 3 compares the algorithms of the different methods. It is evident from Table 3 that the novel network performs better than the current methods. Thus, the results of the suggested Deep Vein Net method are very trustworthy for detecting DVT at an early stage.

5. **CONCLUSION**

This paper presents a novel Deep Vein Net that has been proposed to identify DVT in CT and MRI images. To eliminate noise artifacts, the input CT and MRI images are pre-processed using the DWT. After that, to extract the most pertinent features, the pre-processed images are fed into a Dilated CNN for feature extraction. The pertinent aspects of CT and MRI images are chosen using the STOA. The Fuzzy Extreme Learning Machine classifies the DVT cases and normal instances. The efficacy of the proposed Deep Vein Net was assessed using criteria including F1 score, rec, spe, pre, and acc. The proposed method gives a classification accuracy of 99.25 % for identifying the DVT. The Deep Vein Net advances the overall accuracy by 5.08 %, 8.81 %, and 14.35 % better than PE-Deep Net, Transfer Learning, and DRN, respectively. The proposed method will be improved by combining conventional and deep convolution and modifying its architecture in our future research.

Received on 2 September 2023

REFERENCES

1. H.Y. Ko, *Deep vein thrombosis and pulmonary embolism in spinal cord injuries*, Management and Rehabilitation of Spinal Cord Injuries, Singapore, Springer Nature Singapore, 2022, pp. 513–526.
2. B. Kainz, M.P. Heinrich, A. Makropoulos, J. Oppenheimer, R. Mandegaran, S. Sankar, C. Deane, S. Mischkewitz, F. Al-Noor, A.C. Rawdin, A. Ruttloff, *Non-invasive diagnosis of deep vein thrombosis from ultrasound imaging with machine learning*, NPJ Digital Medicine, **4**, *1*, p. 137 (2021).
3. C. Broderick, L. Watson, M.P. Armon, *Thrombolytic strategies versus standard anticoagulation for acute deep vein thrombosis of the lower limb*, Cochrane Database of Systematic Reviews, **1** (2021).
4. S.M. Kolokotroni, *Deep vein thrombosis and pulmonary embolism following lung resection*, Shanghai Chest, **5**, *33*, pp. 1–5 (2021).
5. S.H. O'Brien, D. Li, L.G. Mitchell, T. Hess, P. Zee, D.L. Yee, J.W. Newburger, L. Sung, V. Rodriguez, *PREVAPIX-ALL: apixaban compared to standard of care for prevention of venous thrombosis in pediatric acute lymphoblastic leukemia (ALL) – rationale and design*, Thrombosis and Haemostasias, **119**, *05*, pp. 844–853 (2019).
6. C. Burton, P. Fink, P. Henningsen, B. Löwe, W. Rief, *Functional somatic disorders: a discussion paper for a new common classification for research and clinical use*, Bmc Medicine, **18**, *1*, pp. 1–7 (2020).
7. E. Muscogiuri, M. Di Girolamo, C. De Dominicis, A. Pisano, C. Palmisano, G. Muscogiuri, A. Laghi, *Pulmonary embolism and computed tomography angiography: Characteristic findings and technical advice*, Imaging, **14**, *1*, pp. 28–37 (2021).
8. M.H. Jalili, T. Yu, C. Hassani, A.E. Prosper, J.P. Finn, A. Bedayat, *Contrast-enhanced MR Angiography without Gadolinium-based contrast material: clinical applications using Ferumoxytol*, Radiology: Cardiothoracic Imaging, **4**, *4*, pp. 210–323 (2022).
9. Y. Zhang, *Machine Learning in Clinical Application of Medical Imaging for Lesion Detection, Segmentation, Diagnosis, Therapy, and Prognosis Prediction*, UC Irvine Electronic Theses and Dissertations, University of California, Irvine, 2020.
10. Y. Huang, *Deep representation and graph learning for disease diagnosis on medical image data*, Hong Kong University of Science and Technology, Hong Kong, 2021.
11. A. Topor, D. Ulieru, C. Ravariu, F. Babarada, *Development of A New One-Eye implant by 3D bioprinting technique*, Rev. Roum. Sci. Techn. – Électrotechn. et Énerg., **68**, *2*, pp. 247–250 (2023).
12. A. Glavan, V. Croitoru, *Incremental learning for edge network intrusion detection*, Rev. Roum. Sci. Techn. – Électrotechn. et Énerg., **68**, *3*, pp. 301–306 (2023).
13. T.H. Xia, M. Tan, J.H. Li, J.J. Wang, Q.Q. Wu, D.X. Kong, *Establish a normal fetal lung gestational age grading model and explore the potential value of deep learning algorithms in fetal lung maturity evaluation*, Chin. Med. J., **134**, *15*, pp. 1828–1837 (2021).
14. K. Kardaras, N. Apostolou, G.I. Lambrou, M. Sarafidis, D. Koutsouris, *development and evaluation of advanced image analysis techniques for pediatric deep vein thrombosis imaging scans*, 19th International Conference on Bioinformatics and Bioengineering (BIBE), IEEE, pp. 296–300, 2019.
15. D. Lynch, M. Suriya, *PE-DeepNet: A deep neural network model for pulmonary embolism detection*, Int. J. Intell. Networks, **3**, pp.176–180 (2022).
16. H. Khachnaoui, M. Agrébi, S. Halouani, N. Khlifa, *deep learning for automatic pulmonary embolism identification using CTA images*, 6th International Conference on Advanced Technologies for Signal and Image Processing (ATSIP), IEEE, pp. 1–6, 2022.
17. M. Khan, P.M. Shah, I.A. Khan, S.U. Islam, Z. Ahmad, F. Khan, Y. Lee, *IoMT-enabled computer-aided diagnosis of pulmonary embolism from computed tomography scans using deep learning*, Sensors, **23**, *3*, p. 1471 (2023).
18. C.Y. Yu, Y.C. Cheng, C. Kuo, *Early pulmonary embolism detection from computed tomography pulmonary angiography using convolutional neural networks*, Joint 9th International Conference on Informatics, Electronics & Vision (ICIEV) and 2020 4th International Conference on Imaging, Vision & Pattern Recognition (icIVPR); IEEE, pp. 1–6, 2020.
19. H. Liu, H. Yuan, Y. Wang, W. Huang, H. Xue, X. Zhang, *Prediction of venous thromboembolism with machine learning techniques in young middle-aged inpatients*, Sci. Rep., **11**, *1*, p. 12868 (2021).
20. K. Gayathri, K. P. Ajitha Gladis, A.A. Mary, *Real-time masked face recognition using deep learning based Yolov4 network*, International Journal of Data Science and Artificial Intelligence, **01**, *01*, pp. 26–32 (2023).
21. J.A. Sajani, A. Ahilan, *Classification of brain disease using deep learning with multi-modality images*, Journal of Intelligent & Fuzzy Systems, Applications in Engineering and Technology, **45**, *2*, pp 3201–3211 (2023).
22. K.B. Shah, S. Visalakshi, R. Panigrahi, *Seven class solid waste management-hybrid features based deep neural network*, International Journal of System Design and Computing, **01**, *01*, pp. 1–10 (2023).